

Reversible hydrogen spillover in Ru-WO_{3-x} enhances hydrogen evolution activity in neutral pH water splitting

Received: 25 April 2022

Accepted: 29 August 2022

Published online: 14 September 2022

Check for updates

Jiadong Chen^{1,2,5}, Chunhong Chen^{1,5}, Minkai Qin^{1,5}, Ben Li¹, Binbin Lin¹, Qing Mao³, Hongbin Yang², Bin Liu^{2,4}✉ & Yong Wang¹✉

Noble metal electrocatalysts (e.g., Pt, Ru, etc.) suffer from sluggish kinetics of water dissociation for the electrochemical reduction of water to molecular hydrogen in alkaline and neutral pH environments. Herein, we found that an integration of Ru nanoparticles (NPs) on oxygen-deficient WO_{3-x} manifested a 24.0-fold increase in hydrogen evolution reaction (HER) activity compared with commercial Ru/C electrocatalyst in neutral electrolyte. Oxygen-deficient WO_{3-x} is shown to possess large capacity for storing protons, which could be transferred to the Ru NPs under cathodic potential. This significantly increases the hydrogen coverage on the surface of Ru NPs in HER and thus changes the rate-determining step of HER on Ru from water dissociation to hydrogen recombination.

Hydrogen, with high gravimetric energy density, is an ideal candidate to replace the traditional fossil fuels and also a pivotal ingredient for essential industrial chemicals (e.g., petroleum refining and ammonia synthesis)^{1–5}. Water electrolysis driven by renewable electricity offers great promises for eco-friendly hydrogen production. Electrolysis of water can be realized in acidic, neutral and alkaline environment, among which, water reduction in neutral/alkaline medium is much more sluggish because of the slow water dissociation reaction^{6–8}. Consequently, even platinum (Pt), the state-of-the-art hydrogen evolution reaction (HER) catalyst, shows two to three orders of magnitude lower activity in neutral/alkaline medium as compared to acidic medium⁹. Although HER in acidic condition exhibits better activity, equipment and catalyst corrosion limit the lifetime of operation. Neutral media provides a more favorable condition for catalysts to remain stable and less corrosive environment for electrolyzers¹⁰. And electrolyzers capable of operating in neutral media offer the possibility of achieving hydrogen production directly from seawater without the need for desalination^{10,11}.

In practical application, catalysts usually operate at large overpotentials to achieve large current densities. In this case, early studies

show that HER in neutral/alkaline medium starts from water dissociation ($M + e^- + H_2O \rightarrow M - H_{ad} + OH^-$, where M refers to the active site and H_{ad} stands for adsorbed H), followed by either the Heyrovsky reaction ($H_2O + e^- + M - H_{ad} \rightarrow M + OH^- + H_2$) or the Tafel reaction ($H_{ad} + H_{ad} \rightarrow H_2$)^{10,12,13}. Compared with HER in acidic environment, the additional splitting of water molecules to supply protons in neutral/alkaline medium is more sluggish in kinetics, resulting in low hydrogen coverage ($M - H_{ad}$) on the surface of the catalyst during HER.

To enhance HER in neutral/alkaline medium, prior approaches were mainly dedicated to facilitating sluggish water dissociation reaction by means of incorporating a specific component (e.g., transition metal hydroxide) onto the catalytically active species (e.g., Pt) or inducing surface reconstruction to expose more active sites^{14–18}. The water dissociation process releases H⁺, which will be bound on the surface of the catalyst, undergoing hydrogen recombination to evolve molecular hydrogen. The sluggish water dissociation reaction in neutral/alkaline medium results in a low H coverage on the surface of HER catalyst, which impedes HER catalysis^{19–21}. Hydrogen spillover, the migration of activated hydrogen atoms generated by the dissociation of di-hydrogen adsorbed on

¹Advanced Materials and Catalysis Group, Center of Chemistry for Frontier Technologies, State Key Laboratory of Clean Energy Utilization, Institute of Catalysis, Department of Chemistry, Zhejiang University, Hangzhou 310028, PR China. ²School of Chemical and Biomedical Engineering, Nanyang Technological University, Singapore 637459, Singapore. ³School of Chemical Engineering, Dalian University of Technology, Dalian 116024 Liaoning, PR China. ⁴Division of Chemistry and Biological Chemistry, School of Physical and Mathematical Sciences, Nanyang Technological University, Singapore 637371, Singapore. ⁵These authors contributed equally: Jiadong Chen, Chunhong Chen, Minkai Qin. ✉e-mail: liubin@ntu.edu.sg; chemwy@zju.edu.cn

a metal surface onto a reducible metal oxide support, is a common phenomenon in heterogeneous catalysis^{22–26}. Recently, hydrogen spillover strategy has been taken into account for the catalysts design to achieve the compelling HER performance, such as Pt alloys-CoP²⁷, Pt/CoP²⁸, and Pt/TiO₂²⁹ electrocatalysts, delivering the optimal HER activity. However, spillover strategies have rarely been studied on neutral HER and the exact mechanism of hydrogen spillover to improve HER is still unclear.

In this work, we develop an effective strategy to significantly increase the H coverage on the catalyst during HER in neutral environment. Specifically, we propose a Ru nanoparticles (NPs) on oxygen-deficient tungsten oxide (Ru-WO_{3-x}) system, in which protons inserted into WO_{3-x} can be transferred to Ru NPs during HER, thereby greatly increasing the hydrogen coverage on Ru NPs and enhancing the HER performance. Through combined in situ Raman spectroscopy investigations, electrochemical measurements and DFT calculations, the hydrogen spillover from WO_{3-x} to Ru NPs during HER has been explicitly demonstrated. Consequently, the HER activity of Ru-WO_{3-x} is enhanced by a factor of 24.0 as compared with the commercial Ru/C (5.0 wt.%) electrocatalyst in 1.0 M phosphate buffer solution (PBS) electrolyte.

Results

Origin of unsatisfied HER activity of Ru/C in neutral medium

Ru, having a lower cost but comparable hydrogen binding energy as compared to Pt^{30–34}, is regarded as one of the good candidates to replace Pt in HER. Early studies demonstrated good HER activity of commercial Ru/C in acidic medium^{35,36}. However, the HER activity of Ru/C significantly reduced in neutral environment. To figure out the sluggish kinetics of HER on Ru/C in neutral medium, we performed microkinetic analysis. The HER activity of commercial Ru/C (5.0 wt.%) electrocatalyst was first evaluated in 1.0 M PBS (Fig. 1a). The Ru/C electrocatalyst displays a large overpotential of 86 mV at a current density of 10 mA cm⁻² with a Tafel slope as large as 78 mV dec⁻¹. By fitting the electrochemical data using a microkinetic model, the HER on Ru/C in neutral medium was found to be rate-limited at the water dissociation step, which led to the low hydrogen coverage (θ_H) on the surface of Ru during HER (Fig. 1b, Supplementary Note 1, Supplementary Tables 1–6, and Supplementary Figs. 1 and 2). The low θ_H on Ru/C in HER was experimentally verified by in situ Raman spectroscopy, where no observable peaks appear in the Raman frequency range of Ru-H vibration (Fig. 1c)^{37,38}. Therefore, effective strategies need to be proposed to enhance the HER activity of Ru/C in neutral media.

Oxygen-deficient tungsten oxide (WO_{3-x}) displays the excellent capability of storing protons in water^{39–41}. If the inserted protons in WO_{3-x} are mobile, WO_{3-x} may be used as a proton reservoir to supply H to increase θ_H on Ru during HER, which thus shall promote the HER

kinetics of Ru in neutral medium. Inspired by this possibility, we prepared Ru NPs on oxygen-deficient WO_{3-x} (Ru-WO_{3-x}) electrocatalysts and studied their HER catalysis.

Synthesis and characterization of Ru-WO_{3-x}

Ru-WO_{3-x} was prepared by a three-step method as schematically illustrated in Fig. 2a. WO₃/CP was first synthesized by a simple hydrothermal method and then impregnated in RuCl₃ solution, followed by a heat treatment in H₂/Ar mixed atmosphere (10/90 molar ratio) to form Ru-WO_{3-x}/CP. The crystal structure of the as-prepared Ru-WO_{3-x}/CP catalyst was examined by X-ray diffraction (XRD) as shown in Fig. 2b. The Ru-WO_{3-x}/CP displays clear diffraction peaks of hexagonal WO₃ (JCPDS No. 85–2460)⁴², but no diffraction peaks related to Ru NPs, possibly due to their small sizes and low content. In addition, the peaks of Ru-WO_{3-x}/CP are shifted to high angles, indicating lattice shrinkage, which may be caused by oxygen vacancies⁴⁰. Scanning electron microscopy (SEM) and transmission electron microscopy (TEM) measurements were performed to probe the morphological information. The WO₃/CP exhibits nanowires with smooth surfaces grown on carbon fibers (Supplementary Fig. 3a–d). High-resolution TEM (HRTEM) image of a single nanowire gives a lattice spacing of 3.84 Å (Supplementary Fig. 3e)^{43,44}, which is attributed to the (002) facet of hexagonal WO₃ (JCPDS No. 85–2460). Energy dispersive X-ray spectroscopy (EDX) elemental mapping of a single WO₃ nanowire reveals uniform distribution of the W and O elements (Supplementary Fig. 3f–h). Comparatively, the Ru-WO_{3-x}/CP displays rough nanowires (Supplementary Fig. 4a, b), indicating successful loading of Ru NPs, which is further verified by the TEM measurements (Supplementary Fig. 4c–e). Both lattice spacings resulting from hexagonal WO₃ and hexagonal Ru are clearly visible in the HRTEM images of Ru-WO_{3-x}/CP (Fig. 2c, d and Supplementary Fig. 4f). On the other hand, the lattice fringes of WO₃ at the edge become blurred, which may be due to the formation of oxygen vacancies induced by hydrogen reduction⁴⁵. EDX elemental mappings reveal uniform distribution of Ru, W and O elements (Supplementary Fig. 4g). Moreover, the average size of the Ru NPs on Ru-WO_{3-x}/CP is 3.5 nm (Supplementary Fig. 4h). The mass content of Ru in Ru-WO_{3-x}/CP was determined to be 5.1 wt.% by inductively coupled plasma optical emission spectrometry (ICP-OES) (Supplementary Table 7). The formation of oxygen vacancies in Ru-WO_{3-x}/CP was confirmed by the electron paramagnetic resonance (EPR) measurement as shown in Fig. 2e. To probe the valence states and further explore the oxygen vacancies in Ru-WO_{3-x}/CP, X-ray photoelectron spectroscopy (XPS) was performed. Ru 3d_{5/2} core level XPS spectrum displays two peaks at 280.28 eV and 281.28 eV, respectively, matching well with Ru(0) and Ru(IV) (Fig. 2f)^{30,31}. The Ru 3p XPS spectrum shows two pairs of peaks, in which the dominant peaks at 461.88 eV and 484.14 eV can be assigned to Ru 3p_{3/2} and Ru 3p_{1/2} of Ru(0) and the rest of the peaks are from Ru(IV), manifesting that the Ru precursor has

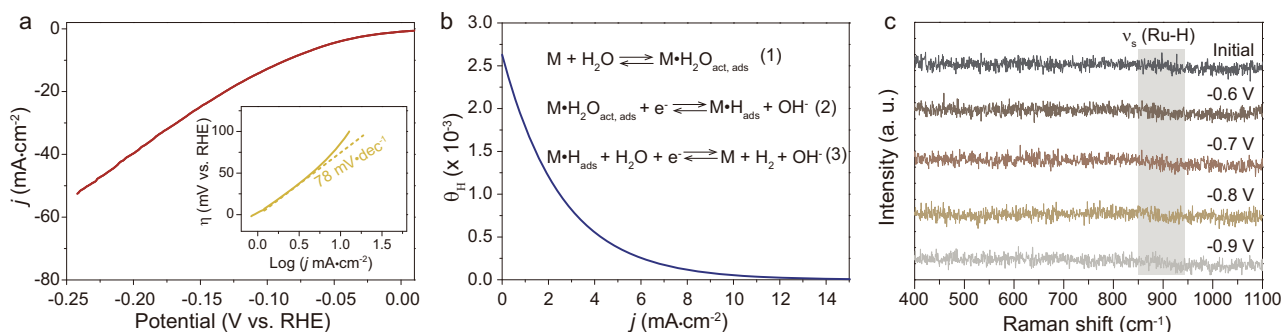


Fig. 1 | HER performance of commercial Ru/C (5 wt%) in 1.0 M PBS. **a** LSV curve and the corresponding Tafel plot for commercial Ru/C (5.0 wt.%) loaded on CP. Scan rate: 2 mV/s. **b** Hydrogen coverage as a function of current density obtained

from the microkinetic analysis. The microkinetic model was built based on three elementary reactions. **c** In situ Raman spectra recorded on Ru/C (5.0 wt.%) in 1.0 M PBS in the potential range from -0.6 to -0.9 V vs. Ag/AgCl.

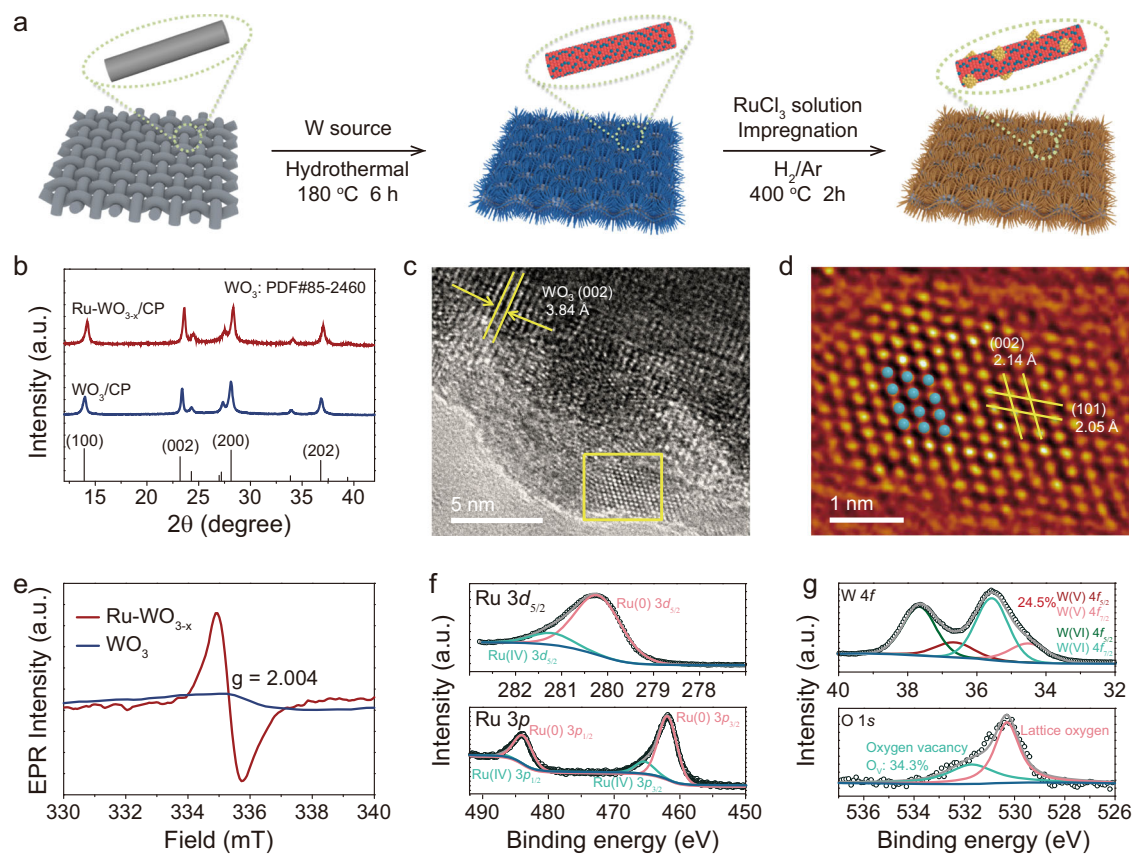


Fig. 2 | Preparation and characterization of Ru-WO_{3-x}/CP. **a** Schematic illustration showing the procedure to prepare Ru-WO_{3-x}/CP. **b** XRD patterns of WO₃/CP and Ru-WO_{3-x}/CP. **c** HRTEM image of Ru-WO_{3-x}/CP. **d** Filtered HRTEM image (using ASBF filter) and the corresponding structural model of Ru nanoparticle marked in

c of Ru-WO_{3-x}/CP. The blue spheres represent Ru atoms. **e** EPR spectra of WO₃ and Ru-WO_{3-x}. **f** Ru 3d_{5/2} and Ru 3p XPS spectra of Ru-WO_{3-x}/CP. **g** W 4f and O 1s XPS spectra of Ru-WO_{3-x}/CP.

been successfully reduced to metallic Ru. The W 4f XPS spectrum of Ru-WO_{3-x}/CP displays two peaks at 35.58 eV and 37.68 eV, which correspond well to the W 4f_{7/2} and W 4f_{5/2} of W(VI), respectively (Fig. 2g)^{40,41}. Additionally, two more deconvoluted peaks at 34.53 eV and 36.63 eV can be assigned to W(V)^{43,45}. Notably, a few hydrogen atoms may be induced in the surface of WO_{3-x} support in the H₂/Ar reduction process and this may also lead to the appearance of W(V). In O 1s XPS spectrum, two deconvoluted peaks are observed. The peak centered at 531.70 eV is assigned to the OH groups or a lattice oxygen bounded to a W(V) atom (close to a vacancy)⁴⁵. And another peak at 530.30 eV is ascribed to the lattice oxygen. The percentage of oxygen vacancies in Ru-WO_{3-x}/CP is determined to be around 34.3%, consistent with the W(V) content deduced from W 4f XPS spectrum. In addition, WO_{3-x}/CP was prepared, and the corresponding W 4f and O 1s XPS spectra of WO_{3-x}/CP showed that there were also a large number of oxygen vacancies (Supplementary Fig. 5). To further investigate oxygen vacancies in Ru-WO_{3-x} and WO_{3-x}, we conducted O₂-temperature programmed desorption (O₂-TPD). The corresponding result reveals oxygen vacancies in WO_{3-x} and Ru-WO_{3-x}, which matches well with the EPR and O 1s XPS results (Supplementary Fig. 6).

HER performance of Ru-WO_{3-x}/CP in neutral media

The HER performance of the as-prepared electrocatalysts was examined in a three-electrode system in N₂ saturated 1.0 M PBS. In comparison to WO_{3-x}/CP and commercial Ru/C (5.0 wt.%)/CP, the Ru-WO_{3-x}/CP exhibits a greatly improved HER activity, reaching a current density of 10 mA cm⁻² at an overpotential as low as 19 mV (Fig. 3a). Notably, the current density of Ru-WO_{3-x}/CP is enhanced by a factor of 24.0 as compared to the commercial Ru/C (5.0 wt.%)/CP at the

potential of -0.150 V vs. RHE. Meanwhile, the Tafel slope of Ru-WO_{3-x}/CP also significantly reduces to 41 mV dec⁻¹ (Fig. 3b), manifesting a change of the rate-determining step (RDS) of HER from water dissociation for Ru/C to hydrogen recombination for Ru-WO_{3-x}^{46,47}. It is noteworthy that the Ru-WO_{3-x}/CP is among the best HER electrocatalysts reported in the neutral medium (Fig. 3c and Supplementary Table 8). Moreover, we also calculated the LSV curves normalized by the electrochemically active surface area and Ru-WO_{3-x}/CP still shows much better HER activity than Ru/C (5.0 wt.%)/CP (Supplementary Figs. 7 and 8). The HER activity and stability under higher current densities were also evaluated. As shown in Supplementary Fig. 9, Ru-WO_{3-x}/CP displays a low overpotential of 225 mV to achieve a current density of 1 A cm⁻², and the potential of Ru-WO_{3-x}/CP remains stable to attain 1 A cm⁻² in the chronopotentiometry test. Besides activity, the Ru-WO_{3-x}/CP also displays excellent durability in catalyzing HER (Fig. 3d). Both the structure and composition of Ru-WO_{3-x}/CP remain unchanged before and after the HER stability test as examined by SEM, HRTEM and ICP-OES (Supplementary Fig. 10 and Supplementary Table 7). Moreover, to explore whether oxygen vacancies have an effect on the HER activity, Ru-WO₃/CP was also synthesized for comparison. As shown in Supplementary Fig. 11, the HER activity of Ru-WO₃/CP is better than that of Ru/C (5.0 wt.%)/CP, but is still much worse than that of Ru-WO_{3-x}/CP. The corresponding Tafel plots indicate that the reaction kinetics of Ru-WO₃/CP is slower than that of Ru-WO_{3-x}/CP, but faster than that of Ru/C (5.0 wt.%)/CP. These results suggest that oxygen-deficient tungsten oxide is beneficial for activity improvement. Moreover, Ru-WO₃/CP keeps stable in the long-term stability test, and no obvious HER activity decay is observed. In addition, WO₃ or WO_{3-x} gradually dissolves in alkaline electrolyte^{48,49}. Thus,

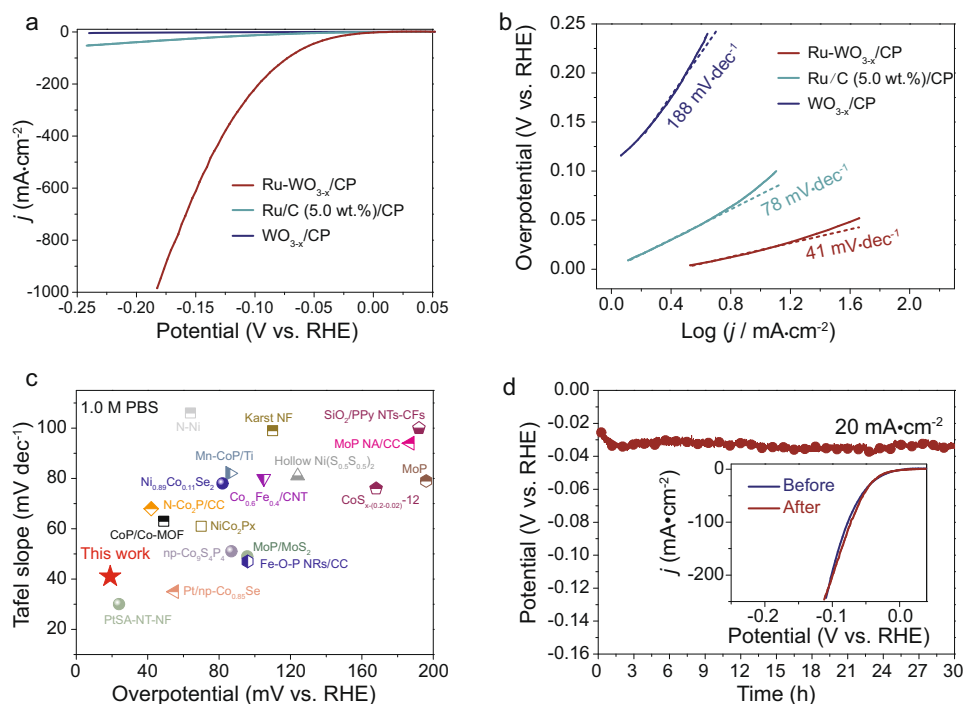


Fig. 3 | HER performance in 1.0 M PBS. a LSV curves in 1.0 M PBS. **b** The corresponding Tafel plots. **c** HER activity comparison of Ru-WO_{3-x}/CP with other reported state-of-the-art electrocatalysts in 1.0 M PBS. The corresponding

references for these reported electrocatalysts are shown in Supplementary Table 8. **d** Chronopotentiometric curve recorded at a constant cathodic current density of 20 mA cm⁻². Inset compares the LSV curves before and after the stability test.

it is not appropriate to apply Ru-WO_{3-x} in alkaline condition because of the stability issue.

To dig out the origin of the enhanced HER activity of Ru-WO_{3-x}/CP, we first examined the tungsten oxide support. According to previous reports, creating oxygen vacancies in tungsten oxide could increase its capacitance^{40,41}. Since proton storage in tungsten oxide is positively correlated with its capacitive performance, gravimetric capacitance of Ru-WO_{3-x}, WO_{3-x} and WO₃ were calculated from cyclic voltammetry (CV) measurements. Here, we separated the capacitive and diffusion-controlled contribution in the measured capacitance using the following equation: $i(V) = k_1v + k_2v^{1/2}$, where $i(V)$, k_1v , and $k_2v^{1/2}$ are total current, capacitive current and diffusion-controlled current in CV, respectively³⁹. The results at various scan rates show that the capacitance of WO_{3-x} is enhanced by a factor of around 23.0 as compared to that of WO₃ (Supplementary Figs. 12–17). Loading Ru NPs onto WO_{3-x} could further increase the capacitance to some extent. The proton insertion/extraction kinetics was assessed using the equation: $i = av^b$, where i is the current response, a is an adjustment coefficient, v is the sweep rate and the power exponent b is a parameter to analyze the kinetics^{50,51}. A b value of 0.5 means diffusion-controlled kinetics and a b value of 1.0 indicates an ideal capacitive or non-diffusion-controlled behavior. By plotting $\log(i)$ vs. $\log(v)$, the b value of Ru-WO_{3-x} is estimated to be 0.99 and 0.82 (Supplementary Fig. 13a, b), respectively, based on the oxidation and reduction redox peak, indicating the dominant pseudocapacitive behavior of proton extraction/insertion and that the proton extraction is more rapid than its insertion in Ru-WO_{3-x}.

To study the HER process, in situ Raman spectroscopy was performed. The in situ Raman spectra of Ru-WO_{3-x}/CP were collected in the potential range from -0.1 to -0.7 V (vs. Ag/AgCl), which includes both the non-Faradaic current region and the HER region. For the initial state at open circuit, the typical Raman peaks of WO_{3-x} were observed at 778 cm⁻¹ (Fig. 4a), which is attributed to the W-O stretching vibration^{45,52}. The Raman signal at 778 cm⁻¹ gradually decreased with increasing applied cathodic potential and this signal completely

disappeared at -0.5 V (vs. Ag/AgCl), due to proton insertion in WO_{3-x}^{53,54}. Additionally, a new Raman peak at 878 cm⁻¹ appeared after the applied potential reached -0.6 V (vs. Ag/AgCl) and the intensity of this peak further increased with increase in applied cathodic potential. Based on previous reports, the Raman peak at 878 cm⁻¹ may result from the Ru-H stretching vibration^{37,38}. To figure out the attribution of the Raman peak at 878 cm⁻¹, a deuterium isotopic substitution experiment was performed. Once H₂O was changed to D₂O, the Raman peak at 878 cm⁻¹ shifted to a lower wavenumber at 611 cm⁻¹ (Fig. 4b). The downward shift ratio (γ) in the isotopic substitution experiment can be estimated by: $\gamma = \nu(\text{Ru-D})/\nu(\text{Ru-H})$ (see details in Supplementary Note 2). The estimated downward shift ratio (γ) of the Ru-H peak is ~71.0%, very close to the theoretical 70.0%. Furthermore, DFT calculation was performed to determine the vibrational frequency of H* on metallic Ru. Here, we considered two Ru models. The Raman frequency of the Ru-H stretching vibration was calculated to be 875 and 880 cm⁻¹ for the ridge and top sites on the Ru cluster (Fig. 4c). These results corroborate the attribution of the Raman peak at 878 cm⁻¹ to the Ru-H stretching vibration. When the potential was swept back from -0.6 V to -0.2 V (vs. Ag/AgCl) in 1.0 M PBS, the characteristic Raman peak of W-O stretching vibration re-appeared at -0.5 V (vs. Ag/AgCl) and the peak intensity increased with further decrease in the cathodic potential, suggesting that the proton extraction started at -0.5 V (vs. Ag/AgCl) (Fig. 4d). Notably, when the applied cathodic potential was increased, the Raman peak intensity of Ru-H first remained steady until -0.5 V (vs. Ag/AgCl) and then gradually increased, suggesting increase of hydrogen coverage on Ru, which may result from proton transfer from WO_{3-x} to Ru NPs. Moreover, the deuterium isotopic substitution experiment should also be performed on WO_{3-x}/CP. As shown in Supplementary Fig. 18, there is no obvious difference between the Raman results in deuterium isotopic substitution and non-deuterium isotopic substitution experiments. Only W-O Raman peaks can be seen in the Raman spectra.

Furthermore, the hydrogen coverage (θ_H) on Ru-WO_{3-x}/CP in HER was studied by microkinetic analysis (Supplementary Note 1,

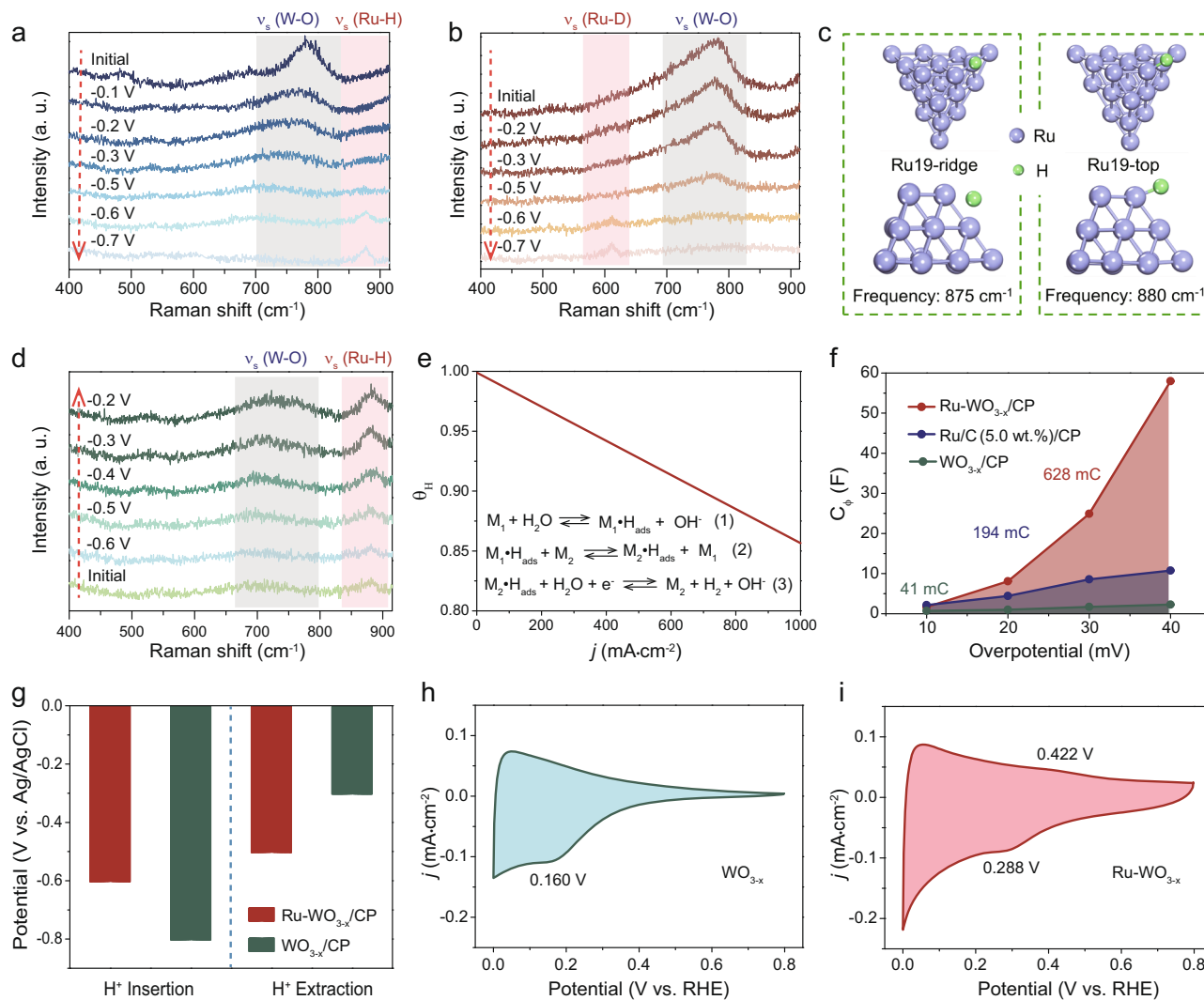


Fig. 4 | Insights of hydrogen spillover. **a** In situ Raman spectra of Ru-WO_{3-x}/CP recorded in 1.0 M PBS from -0.1 to -0.7 V vs. Ag/AgCl. **b** In situ Raman spectra of Ru-WO_{3-x}/CP recorded from -0.2 to -0.7 V vs. Ag/AgCl in 1.0 M PBS (in D₂O). **c** Side and top view illustrations of DFT models used for Raman frequency calculation of Ru-H vibration. **d** In situ Raman spectra of Ru-WO_{3-x}/CP recorded in 1.0 M PBS from -0.6 to -0.2 V vs. Ag/AgCl. **e** Hydrogen coverage as a function of current density

obtained from microkinetic analysis. **f** Fitted data of C_{dl} at different overpotentials for various electrocatalysts during HER in 1.0 M PBS. **g** The onset potential of H⁺ insertion and extraction for Ru-WO_{3-x}/CP and WO_{3-x}/CP. **h** CV curve of WO_{3-x} recorded in 1.0 M PBS. Scan rate: 5 mV/s. **i** CV curve of Ru-WO_{3-x} recorded in 1.0 M PBS. Scan rate: 5 mV/s.

Supplementary Tables 1–6, and Supplementary Figs. 1 and 2). Compared with θ_H on Ru/C (5.0 wt.%)/CP (Fig. 1b), θ_H on Ru-WO_{3-x}/CP significantly increases (Fig. 4e), matching well with the in situ Raman spectra (Figs. 1c and 4a). Operando electrochemical impedance spectroscopy (EIS) measurement was further conducted to probe the hydrogen adsorption/desorption process in HER^{27,53}. The obtained EIS data was simulated using an equivalent circuit model as shown in Supplementary Fig. 19 and Supplementary Table 9. The first parallel circuit, with one resistor (R_c) and one constant phase element (CPE_1), corresponds to the inner layer of electrode material, where R_c is the charge transfer resistance and CPE_1 corresponds to the double-layer capacitance. The second parallel circuit simulates the electrolyte-catalyst interfacial charge transfer^{27,55,56}, which is able to reflect the hydrogen intermediate adsorption behavior on the catalytically active sites (R_i is the charge transfer resistance and C_p represents the hydrogen adsorption pseudo-capacitance). C_p as a function of overpotential was integrated to calculate the hydrogen adsorption charge (Q_H). Compared with Q_H for Ru/C (5.0 wt.%)/CP, Q_H (originated from Ru) ($Q_H^{(Ru-WO_{3-x}/CP)} - Q_H^{(WO_{3-x}/CP)}$) for Ru-WO_{3-x}/CP increases a lot (Fig. 4f), in good agreement with

the greatly increased θ_H on Ru-WO_{3-x}/CP deduced from microkinetic analysis.

To explore factors that influence proton insertion/extraction in tungsten oxide, in situ Raman measurements were also performed on WO_{3-x}/CP (Supplementary Fig. 20). By comparing the onset potential of proton insertion/extraction, it is found that introduction of Ru onto WO_{3-x} results in a more positive onset potential for proton insertion while a more negative onset potential for proton extraction (Fig. 4g). This indicates that Ru NPs can not only promote proton insertion but also accelerate proton extraction from WO_{3-x}. Furthermore, CV was performed in 1.0 M PBS to investigate the proton insertion/extraction behavior (Fig. 4h, i). In the CV curves, obvious proton insertion peaks are observed on WO_{3-x} at 0.160 V (vs. RHE) and Ru-WO_{3-x} at 0.288 V (vs. RHE)^{39,40}. Furthermore, a distinct proton extraction peak at 0.422 V (vs. RHE) can be observed on Ru-WO_{3-x}, but not on WO_{3-x}, strongly illustrating that Ru NPs can promote proton extraction from WO_{3-x}.

Theoretical insights of reversible hydrogen spillover in HER

To gain some theoretical insights on whether hydrogen spillover can take place from WO_{3-x} to Ru NPs, DFT calculations were carried out to

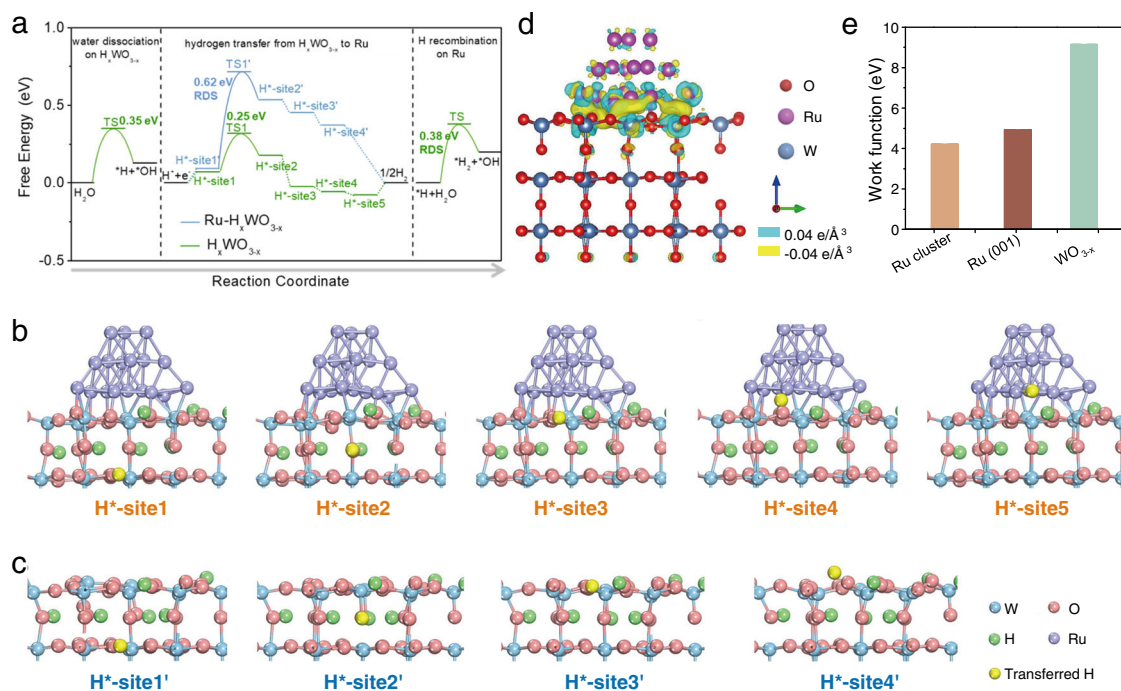


Fig. 5 | DFT calculations of hydrogen transfer energy barrier. a Calculated free energy diagram for HER on $Ru-H_xWO_{3-x}$ and H_xWO_{3-x} . **b** The optimized H^+ adsorption structure on various sites of $Ru-H_xWO_{3-x}$. **c** The optimized H^+ adsorption structure on various sites of H_xWO_{3-x} . **d** Electron density difference

plot across the $Ru-WO_{3-x}$ interface. Electron accumulation and depletion are indicated in yellow and blue, respectively. **e** Work function calculations for various Ru and WO_{3-x} .

determine the hydrogen transfer energy barrier. The Gibbs free energy change at each step of hydrogen transfer from the interior of WO_{3-x} to the surface of Ru NPs was computed. As hydrogen spillover occurs on proton-inserted WO_{3-x} (H_xWO_{3-x}), a moderate amount of H was added into the as-built WO_{3-x} model to simulate the actual situation. As shown in Fig. 5a–c, hydrogen adsorption is extremely weak on the external surface of H_xWO_{3-x} (site 2, 3 and 4), while it becomes much stronger on the inner surface (site 1), suggesting that interior of H_xWO_{3-x} is more favorable for hydrogen adsorption. The difference of hydrogen adsorption between internal and external surface results in a large difference in Gibbs free energy of adsorbed hydrogen (ΔG_{H^+}) between site 1 and site 2, with a thermodynamic barrier of 0.44 eV. Meanwhile, the kinetic barrier of hydrogen transfer from site 1 to site 2 was calculated to be 0.62 eV, indicating difficulty of hydrogen transfer from site 1 to site 2. On the contrary, ΔG_{H^+} values of site 2, 3 and 4 on $Ru-H_xWO_{3-x}$ become more negative, suggesting much improved hydrogen adsorption on the external surface of $Ru-H_xWO_{3-x}$. Benefitted from the enhanced hydrogen adsorption, the thermodynamic barrier of hydrogen transfer from site 1 to site 2 reduces to 0.11 eV. Furthermore, the kinetic hydrogen transfer barrier (from site 1 to site 2 on $Ru-H_xWO_{3-x}$) was calculated to be 0.25 eV, manifesting that the hydrogen transfer process is greatly promoted on $Ru-H_xWO_{3-x}$. Additionally, it is found that the hydrogen adsorption on Ru surface (site 5) is stronger than that on H_xWO_{3-x} , as indicated by the most negative ΔG_{H^+} of -0.078 eV on site 5. Therefore, the adsorbed hydrogen can be spontaneously transferred from external surface of H_xWO_{3-x} to Ru (from site 4 to site 5). To unravel the facilitated hydrogen transfer process on $Ru-WO_{3-x}$, the charge density difference was calculated to explore the charge distribution at the interface. As shown in Fig. 5d, electron accumulation is observed below the surface layer of WO_{3-x} . High density electrons are favorable to trap hydrogen atoms via interacting with unsaturated electrons in the H 1s orbital. Therefore, hydrogen adsorption is significantly enhanced on the external surface of WO_{3-x} . Moreover, electron accumulation below the surface layer of

WO_{3-x} also attracts protons in the interior to the surface by electrostatic interaction. As a result, hydrogen spillover from WO_{3-x} to Ru is thermodynamically and kinetically facilitated. Next, to investigate the cause of charge transfer between Ru NPs and WO_{3-x} , the work functions (ϕ) of Ru and WO_{3-x} were calculated. The work function of Ru NPs was determined to be 4.91 eV, much smaller than that of WO_{3-x} (9.14 eV), revealing electron transfer from Ru to WO_{3-x} (Fig. 5e and Supplementary Figs. 21 and 22). Taking into account the size distribution of Ru NPs, the work function of bulk Ru was also computed, which is slightly larger than that of Ru NPs but still much smaller than that of WO_{3-x} . Combining with the above analyses, a reasonable explanation for hydrogen spillover from WO_{3-x} to Ru is given as follows: the difference in work function between Ru NPs and WO_{3-x} leads to electron accumulation at the subsurface of WO_{3-x} , which enhances hydrogen adsorption and also drives moving internal protons to the external surface. In addition, DFT calculations were also performed to reveal the free energy change in H transfer and the electronic structure of $Ru-WO_3/CP$ (Supplementary Fig. 23). The free energy change in H transfer of $Ru-WO_3/CP$ is comparable to that of $Ru-WO_{3-x}/CP$, and the kinetic energy barrier of $Ru-WO_3/CP$ from site 1 to site 2 is determined to be 0.31 eV, only slightly higher than that of $Ru-WO_{3-x}/CP$, indicating that H transfer is also favorable on $Ru-WO_3/CP$. The charge difference of $Ru-WO_3/CP$ also reveals that electrons transfer from Ru to WO_3 , which is the same as that of $Ru-WO_{3-x}/CP$.

To explore the RDS of HER on $Ru-H_xWO_{3-x}$, we conducted DFT calculations to investigate the energy barrier of reaction steps. It is well-known that water dissociation is the RDS in alkaline and neutral media water oxidation, which can be deduced from the very large Tafel slopes. The Heyrovsky reaction and Tafel reaction are closely correlated with the Gibbs free energy of adsorbed hydrogen (ΔG_{H^+}), which is the typical HER descriptor. We calculated the energy barrier of water dissociation and the ΔG_{H^+} on various sites to explore the RDS of HER taking place on $Ru-H_xWO_{3-x}$. As revealed in Supplementary Figs. 24–26, the barrier for water dissociation on Ru is about 0.46 eV

and that on WO_{3-x} is around 0.35 eV. The water dissociation on WO_{3-x} is more favorable than that on Ru. As the further increase of overpotential, WO_{3-x} will dissociate the water to generate protons, which can also spillover to Ru. The OH on the surface of WO_{3-x} will undergo desorption and then be quickly captured by the buffer electrolyte. The OH concentration on the catalyst's surface is low because the buffer electrolyte can react quickly with the desorbed OH to produce H_2O . As shown in Supplementary Figs. 27 and 28, the ΔG_{H^+} on the corner and edge sites of Ru clusters of $\text{Ru-H}_x\text{WO}_{3-x}$ are close to 0 eV, which is the thermodynamically neutral state. To further explore the reaction process, we calculated the energy barriers of the Tafel step and Heyrovsky step on Ru, respectively. As shown in Supplementary Figs. 29–31, the Heyrovsky step shows a lower energy barrier than the Tafel step, suggesting that the hydrogen atoms on Ru transferred from WO_{3-x} tend to follow the Heyrovsky mechanism to generate di-hydrogen. As the energy barrier of hydrogen transfer from WO_{3-x} to Ru is only 0.25 eV, the whole process to generate di-hydrogen including hydrogen atoms spillover from WO_{3-x} to Ru followed by the Heyrovsky step to generate di-hydrogen has an energy barrier of 0.38 eV, indicating Heyrovsky step is the rate limiting step in this process (Fig. 5a). However, the di-hydrogen produced by water dissociation over Ru itself has a higher energy barrier of 0.46 eV, suggesting that this process is more difficult than the spillover mechanism to generate molecular hydrogen. Therefore, the H atoms involved in the reaction tend to come from H transfer from $\text{Ru-H}_x\text{WO}_{3-x}$ to Ru rather than water dissociation on Ru of $\text{Ru-WO}_{3-x}/\text{CP}$.

Based on the above investigations, a possible mechanism is proposed to account for the greatly enhanced HER activity of Ru-WO_{3-x} in neutral medium (Fig. 6). Under applied cathodic potential, protons in the electrolyte were inserted into the oxygen-deficient WO_{3-x} and then coupled with electrons to form $\text{H}_x\text{WO}_{3-x}$. The plenty of oxygen vacancies in WO_{3-x} significantly increased the proton storage capacity and at the same time improved the charge transfer. As a result, the oxygen-deficient WO_{3-x} served as a proton reservoir to supply protons onto Ru surface, which recombined to evolve molecular hydrogen. As the further increase of overpotential, WO_{3-x} will dissociate the water to generate protons, which also spilled over to Ru. The hydrogen spillover from WO_{3-x} to Ru changed the RDS of HER on Ru in neutral medium from water dissociation to hydrogen recombination, which greatly improved the HER kinetics (denoted as pathway 1). In addition, hydrogen recombination on $\text{H}_x\text{WO}_{3-x}$ (denoted as pathway 2) and hydrogen formation on Ru NPs (denoted as pathway 3), where hydrogen is all provided by water dissociation on Ru, are both unfavorable.

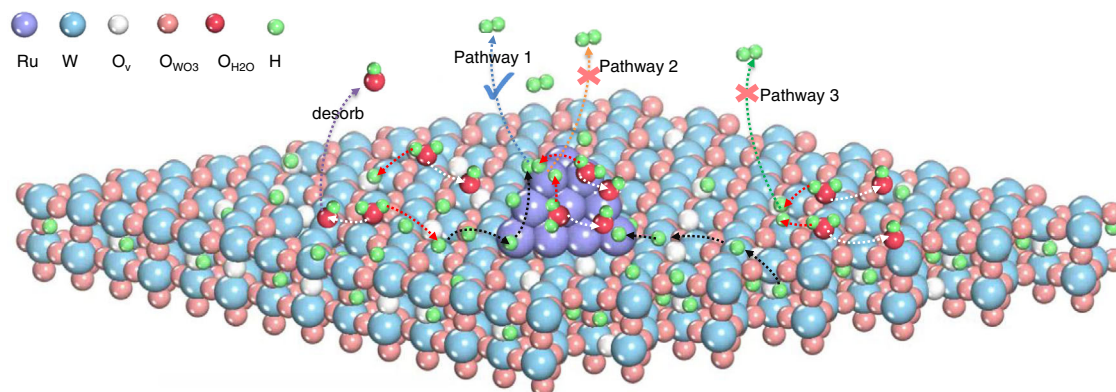


Fig. 6 | Illustration of hydrogen spillover. Schematic diagram showing how hydrogen spillover from WO_{3-x} to Ru enhances HER in neutral environment. The white and red arrows indicate the formation process of OH and H from the dissociation of water, respectively. Black arrows indicate the transfer process of H. The

Discussion

In summary, we report the design and performance of Ru-WO_{3-x} to facilitate different parts of the multistep HER process in neutral environment: the oxygen-deficient WO_{3-x} possesses a large capacity for storing protons, which can be transferred to the surface of Ru NPs under cathodic potential. This hydrogen spillover from WO_{3-x} to Ru changes the RDS of HER on Ru in neutral medium from water dissociation to hydrogen recombination, which greatly improves the HER kinetics.

Methods

Materials

Ruthenium (III) chloride anhydrous (RuCl_3) and ammonium metatungstate hydrate ($(\text{NH}_4)_6\text{H}_2\text{W}_{12}\text{O}_{40}\cdot x\text{H}_2\text{O}$) with 99.5% metals basis were purchased from Shanghai Macklin Biochemical Co., Ltd. Potassium phosphate monobasic (KH_2PO_4 , AR, 99.5%) and potassium hydrogen phosphate (K_2HPO_4 , $\geq 98\%$, ACS) were obtained from Shanghai Aladdin Bio-Chem Technology Co., Ltd. The TGP-H-060 TORAY carbon paper (CP) was purchased from Suzhou Sinero Technology Co., Ltd. The ethanol ($\text{CH}_3\text{CH}_2\text{OH}$, AR, $\geq 99.5\%$) and acetone ($\text{C}_3\text{H}_6\text{O}$, AR, $\geq 95\%$) were purchased from Sinopharm Chemical Reagent Co., Ltd. Nickel(II) acetate tetrahydrate ($\text{Ni}(\text{O}-\text{COCH}_3)_2\cdot 4\text{H}_2\text{O}$, AR, 98%), chloroplatinic acid hexahydrate ($\text{H}_2\text{PtCl}_6\cdot 6\text{H}_2\text{O}$, ACS reagent, $\geq 37.50\%$ Pt basis), sodium borohydride (NaBH_4 , granular, 99.99% trace metals basis), sodium hydroxide (NaOH , ACS reagent, $\geq 97.0\%$, pellets), and molybdenum(VI) oxide (MoO_3 , nanopowder, 100 nm (TEM), 99.5% trace metals basis) were purchased from Sigma-Aldrich. All chemicals were used as received with purification. Ultrapure water (deionized) was used in all the experiments.

Preparation of WO_3/CP

A piece of CP ($4\text{ cm} \times 3\text{ cm} \times 0.19\text{ mm}$) was cleaned by ultrasonication in acetone for 15 min, and then dried in air. $(\text{NH}_4)_6\text{H}_2\text{W}_{12}\text{O}_{40}\cdot x\text{H}_2\text{O}$ (4.0 mmol, 11.825 g) was dissolved in 60.0 ml ultrapure water, followed by magnetic stirring for 20 min to obtain a homogeneous solution. The above solution was transferred into a 100 ml autoclave and CP was placed vertically in the solution. Then, the autoclave was heated at 180°C for 16 h. The obtained WO_3/CP was washed in deionized water and dried at 70°C overnight.

Preparation of $\text{WO}_{3-x}/\text{CP}$

WO_3/CP ($1\text{ cm} \times 1.5\text{ cm}$) was annealed at 400°C for 2 h at a heating rate of $5^\circ\text{C}/\text{min}$ in H_2/Ar (10/90) atmosphere to obtain $\text{WO}_{3-x}/\text{CP}$.

purple arrow indicates the desorption of OH adsorbed on the surface. The blue, orange and green arrows indicate the different ways of formation of molecular hydrogen.

Preparation of Ru-WO_{3-x}/CP

RuCl₃ (40.0 mg) was dissolved in 20.0 ml deionized water by magnetic stirring and ultrasonication to obtain 2.0 mg/ml RuCl₃ solution. WO₃/CP (1 cm × 1.5 cm) was immersed in 10 ml 2.0 mg/ml RuCl₃ solution for 2 min. Subsequently, the WO₃/CP was taken out and dried in an infrared desiccator for 8 min to obtain RuCl₃-WO₃/CP. Finally, the RuCl₃-WO₃/CP was annealed at 400 °C for 2 h at a heating rate of 5 °C/min in H₂/Ar (10/90) atmosphere to obtain Ru-WO_{3-x}/CP.

Preparation of Ru-WO₃/CP

NaBH₄ (100.0 mg) was dissolved in 20.0 ml 1.0 M NaOH solution under magnetic stirring to obtain 5.0 mg/ml NaBH₄ solution. WO₃/CP (1 cm × 1.5 cm) was immersed in 10 ml 2.0 mg/ml RuCl₃ solution for 2 min. Subsequently, the WO₃/CP was taken out and dried in an infrared desiccator for 8 min to obtain RuCl₃-WO₃/CP. Finally, RuCl₃-WO₃/CP was immersed in 5.0 mg/ml NaBH₄ solution for 10 min to obtain Ru-WO₃/CP.

Materials characterizations

Power XRD patterns were recorded on a Rigaku Ultima IV (Cu K α radiation, $\lambda = 1.54 \text{ \AA}$) diffractometer at the operating voltage of 40 kV and current of 20 mA. The HRTEM measurement was conducted on a JEOL JEM-2100F with a 200 kV acceleration voltage. XPS spectra were collected on a Thermo Scientific ESCALAB 250Xi with Al K α radiation (1486.6 eV). SEM images were taken on a Hitachi SU8010 microscope. Raman spectroscopy analysis was performed on a JY, HR 800 Raman spectrometer with a 514 nm laser. EPR experiment was conducted on a Bruker A300-10/12. Oxygen temperature programmed desorption (O₂-TPD) analysis was performed on a BELCAT II fully automatic chemisorber instrument (MicrotracBEL). The procedures were as follows: (1) each sample was pretreated under a He flow (50 ml min⁻¹) at 300 °C for 30 min; (2) the sample was purged with 5% O₂/He for 1 h at 50 °C for O₂ adsorption; (3) the sample was heated to 700 °C at a heating rate of 10 °C min⁻¹ under a pure He gas flow. The signal of O₂ desorption was measured by a thermal conductivity detector.

Electrochemical measurements

All of the electrochemical measurements were conducted on a CHI 760E electrochemical workstation (CH Instruments Ins.) in a three-electrode system at room temperature. The geometric area of the CP is 1 cm × 1 cm. A graphite rod electrode and a saturated calomel electrode (SCE) were used as the counter electrode and the reference electrode, respectively. The potential of SCE vs. reversible hydrogen electrode (RHE) was determined by performing CV scans (scan rate: 1 mV/s) in a hydrogen-saturated electrolyte with a Pt plate as both the working and counter electrode, and the average value of the two potentials at the current of zero in the CV curve is regarded as the potential of SCE vs. RHE. Linear sweep voltammetry (LSV) was performed at a scan rate of 2 mV s⁻¹ after purging H₂ in the electrolyte for 20 min. All of the potentials in LSV are iR-corrected. The resistance for iR-compensation was tested at the open circuit potential. EIS was conducted in the frequency range from 10⁵ Hz to 10⁻³ Hz. All potentials are referenced to the RHE by the Nernst equation: $E_{(\text{RHE})} = E_{(\text{SCE})} + 0.0591 \times \text{pH} + 0.242 \text{ V}$, unless otherwise stated. In total, 1.0 M phosphate buffered solution (PBS) was prepared by mixing 1.0 M K₂HPO₄ with 1.0 M KH₂PO₄ in a volume ratio of 2:1. In this work, only the potentials in the Raman spectra are relative to the Ag/AgCl electrode; all other potentials are relative to the RHE.

CV measurements to determine the specific capacitance

As CP has double-layer capacitance, the powders of WO₃, WO_{3-x} and Ru-WO_{3-x}, which were peeled off from WO₃/CP, WO_{3-x}/CP and Ru-WO_{3-x}/CP, were used for the CV measurements. The ink for the working electrode was prepared by dispersing 5 mg of catalyst in a

mixture of 480 μl of ethanol and 20 μl of 5 wt% Nafion solution, followed by sonication for 30 min to obtain a homogeneous dispersion. A 10 μl of the ink was cast on the glassy carbon electrode (5 mm of diameter) and then dried in air; the as-prepared electrode served as the working electrode. A SCE and a graphite rod electrode were used as the reference electrode and the counter electrode, respectively. All of the CV scans were performed after purging N₂ into the electrolyte for 20 min.

In situ Raman spectroscopy measurements

In situ Raman spectra were recorded on a LabRAM HR Evolution (HORIBA Scientific) spectrometer. The electrochemical cell used for Raman measurement was homemade by Teflon and a quartz plate was employed as the window to cross the laser. A Pt wire and an Ag/AgCl electrode (1.0 M KCl as inner filling electrolyte) were applied as the counter electrode and the reference electrode, respectively. To apply a controlled potential on the catalyst during the Raman measurement, chronoamperometry was performed at various potentials in 1.0 M PBS. The illustration of operando Raman spectroscopy setup is shown in Supplementary Fig. 32.

DFT calculation

Density functional theory (DFT) calculations using the plane-wave technique were conducted in the Vienna Ab Initio Simulation Package. The exchange-correlation functional was the Perdew-Burke-Ernzerhof parametrization of the generalized gradient approximation. The electron-ion interactions were described by the projector augmented wave. Van der Waals interactions were corrected by the DFT-D3 method. A plane-wave basis was set with the cutoff energy of 400 eV. The Brillouin zone was built with a (2 × 2 × 1) Monkhoest-Pack k-point mesh for all models in the optimization of the supercell structure. The force residue for relaxation of all the atoms was set as 0.02 eV/Å. The lattice parameter used for hexagonal WO₃ was 7.51 Å × 7.51 Å × 7.71 Å (a × b × c). Gibbs free energy of hydrogen adsorption was calculated by:

$$\Delta G_{\text{H}} = E_{\text{H}/\text{surf}} - E_{\text{surf}} - 1/2 E_{\text{H}_2} + \Delta E_{\text{ZPE}} - T \Delta S_{\text{H}}$$

where $E_{\text{H}/\text{surf}}$ is the total energy of surface with adsorbate, E_{surf} is the energy of clean surface, E_{H_2} is the energy of a gas phase H₂ molecule, ΔE_{ZPE} represents the zero-point energy of the system and was taken as 0.05 eV, and $T \Delta S_{\text{H}}$ is the contribution from entropy and was simplified as 0.20 eV at 298 K. In this work, the final state of the calculated H₂ is in gas phase.

Reporting summary

Further information on research design is available in the Nature Research Reporting Summary linked to this article.

Data availability

The remaining data contained within the paper and Supplementary Files are available from the authors upon request.

References

- Dresselhaus, M. & Thomas, I. Alternative energy technologies. *Nature* **414**, 332–337 (2001).
- Holladay, J. D., Hu, J., King, D. L. & Wang, Y. An overview of hydrogen production technologies. *Catal. Today* **139**, 244–260 (2009).
- Seh, Z. W. et al. Combining theory and experiment in electrocatalysis: insights into materials design. *Science* **355**, eaad4998 (2017).
- Turner, J. A. Sustainable hydrogen production. *Science* **305**, 972–974 (2004).

- Qin, M. et al. Elucidating electrocatalytic mechanism for large-scale cycloalkanol oxidation integrated with hydrogen evolution. *Chem. Eng. J.* **442**, 136264–136274 (2022).
- You, B. et al. Universal surface engineering of transition metals for superior electrocatalytic hydrogen evolution in neutral water. *J. Am. Chem. Soc.* **139**, 12283–12290 (2017).
- Peng, J. et al. Recent advances in 2D transition metal compounds for electrocatalytic full water splitting in neutral media. *Mater. Today Adv.* **8**, 100081–100097 (2020).
- Han, G. H. et al. Micro-nanoporous MoO₂@CoMo heterostructure catalyst for hydrogen evolution reaction. *Appl. Catal., B* **270**, 118895–118904 (2020).
- Subbaraman, R. et al. Enhancing hydrogen evolution activity in water splitting by tailoring Li⁺-Ni(OH)₂-Pt interfaces. *Science* **334**, 1256–1260 (2011).
- Dinh, C.-T. et al. Multi-site electrocatalysts for hydrogen evolution in neutral media by destabilization of water molecules. *Nat. Energy* **4**, 107–114 (2019).
- Zhou, Z. et al. Electrocatalytic hydrogen evolution under neutral pH conditions: current understandings, recent advances, and future prospects. *Energy Environ. Sci.* **13**, 3185–3206 (2020).
- Men, Y. et al. Tailoring the electronic structure of Co₂P by N doping for boosting hydrogen evolution reaction at all pH values. *ACS Catal.* **9**, 3744–3752 (2019).
- Men, Y. et al. Nitrogen-doped CoP as robust electrocatalyst for high-efficiency pH-universal hydrogen evolution reaction. *Appl. Catal. B* **253**, 21–27 (2019).
- Anantharaj, S. et al. Enhancing electrocatalytic total water splitting at few layer Pt-NiFe layered double hydroxide interfaces. *Nano Energy* **39**, 30–43 (2017).
- Yin, H. et al. Ultrathin platinum nanowires grown on single-layered nickel hydroxide with high hydrogen evolution activity. *Nat. Commun.* **6**, 1–8 (2015).
- Wang, P. et al. Precise tuning in platinum-nickel/nickel sulfide interface nanowires for synergistic hydrogen evolution catalysis. *Nat. Commun.* **8**, 1–9 (2017).
- Qin, S. et al. Ternary nickel-tungsten-copper alloy rivals platinum for catalyzing alkaline hydrogen oxidation. *Nat. Commun.* **12**, 1–10 (2021).
- Lu, B. et al. Ruthenium atomically dispersed in carbon outperforms platinum toward hydrogen evolution in alkaline media. *Nat. Commun.* **10**, 1–11 (2019).
- Yang, Y. et al. Hierarchical nanoassembly of MoS₂/Co₉S₈/Ni₃S₂/Ni as a highly efficient electrocatalyst for overall water splitting in a wide pH range. *J. Am. Chem. Soc.* **141**, 10417–10430 (2019).
- Feng, L.-L. et al. High-index faceted Ni₃S₂ nanosheet arrays as highly active and ultrastable electrocatalysts for water splitting. *J. Am. Chem. Soc.* **137**, 14023–14026 (2015).
- Jiang, W.-J., Tang, T., Zhang, Y. & Hu, J.-S. Synergistic modulation of non-precious-metal electrocatalysts for advanced water splitting. *Acc. Chem. Res.* **53**, 1111–1123 (2020).
- Khoobiar, S. Particle to particle migration of hydrogen atoms on platinum-alumina catalysts from particle to neighboring particles. *J. Phys. Chem.* **68**, 411–412 (1964).
- Miu, E. V. & McKone, J. R. Comparisons of WO₃ reduction to H_xWO₃ under thermochemical and electrochemical control. *J. Mater. Chem. A* **7**, 23756–23761 (2019).
- Prins, R. Hydrogen spillover. Facts and fiction. *Chem. Rev.* **112**, 2714–2738 (2012).
- Levy, R. & Boudart, M. The kinetics and mechanism of spillover. *J. Catal.* **32**, 304–314 (1974).
- Roland, U., Braunschweig, T. & Roessner, F. On the nature of spilt-over hydrogen. *J. Mol. Catal. A Chem.* **127**, 61–84 (1997).
- Li, J. Y. et al. A fundamental viewpoint on the hydrogen spillover phenomenon of electrocatalytic hydrogen evolution. *Nat. Commun.* **12**, 3502–3513 (2021).
- Li, J. et al. Ethylene-glycol ligand environment facilitates highly efficient hydrogen evolution of Pt/CoP through proton concentration and hydrogen spillover. *Energy Environ. Sci.* **12**, 2298–2304 (2019).
- Wei, Z. W. et al. Reversed charge transfer and enhanced hydrogen spillover in platinum nanoclusters anchored on titanium oxide with rich oxygen vacancies boost hydrogen evolution reaction. *Angew. Chem. Int. Ed.* **133**, 16758–16763 (2021).
- Wang, J. et al. Highly uniform Ru nanoparticles over N-doped carbon: pH and temperature-universal hydrogen release from water reduction. *Energy Environ. Sci.* **11**, 800–806 (2018).
- Mahmood, J. et al. An efficient and pH-universal ruthenium-based catalyst for the hydrogen evolution reaction. *Nat. Nanotechnol.* **12**, 441–446 (2017).
- Chen, J. et al. Improving alkaline hydrogen evolution reaction kinetics on molybdenum carbide: introducing Ru dopant. *J. Catal.* **392**, 313–321 (2020).
- Chen, J., Wang, H., Gong, Y. & Wang, Y. Directly immobilizing a Ru-tannic acid linkage coordination complex on carbon cloth: an efficient and ultrastable catalyst for the hydrogen evolution reaction. *J. Mater. Chem. A* **7**, 11038–11043 (2019).
- Liu, Y. et al. Ru modulation effects in the synthesis of unique rod-like Ni@Ni₂P-Ru heterostructures and their remarkable electrocatalytic hydrogen evolution performance. *J. Am. Chem. Soc.* **140**, 2731–2734 (2018).
- Li, F. et al. Mechanochemically assisted synthesis of a Ru catalyst for hydrogen evolution with performance superior to Pt in both acidic and alkaline media. *Adv. Mater.* **30**, 1803676 (2018).
- Qin, X. et al. The role of Ru in improving the activity of Pd toward hydrogen evolution and oxidation reactions in alkaline solutions. *ACS Catal.* **9**, 9614–9621 (2019).
- Hagemann, H. & Moyer, R. O. Raman spectroscopy studies on M₂RuH₆ where M= Ca, Sr and Eu. *J. Alloy. Compd.* **330**, 296–300 (2002).
- Hagemann, H. et al. Structural and vibrational properties of Ca₂FeH₆ and Sr₂RuH₆. *J. Phys. Chem. Solids* **72**, 286–289 (2011).
- Jiang, H. et al. Insights on the proton insertion mechanism in the electrode of hexagonal tungsten oxide hydrate. *J. Am. Chem. Soc.* **140**, 11556–11559 (2018).
- Park, J. et al. Investigation of the support effect in atomically dispersed Pt on WO_{3-x} for utilization of Pt in the hydrogen evolution reaction. *Angew. Chem. Int. Ed.* **58**, 16038–16042 (2019).
- Huang, Z. H. et al. Electrical and structural dual function of oxygen vacancies for promoting electrochemical capacitance in tungsten oxide. *Small* **16**, 2004709 (2020).
- Gong, H. et al. Preparation and supercapacitive property of molybdenum disulfide (MoS₂) nanoflake arrays-tungsten trioxide (WO₃) nanorod arrays composite heterojunction: a synergistic effect of one-dimensional and two-dimensional nanomaterials. *Electrochim. Acta* **263**, 409–416 (2018).
- Wang, L., Liu, Y., Han, G. & Zhao, H. Controllable synthesis of hexagonal WO₃ nanorod-cluster films with high electrochromic performance in NIR range. *J. Alloy. Compd.* **890**, 161833 (2022).
- Shen, L., Luo, G., Zheng, J. & Xu, C. Effect of pH on the electrochromic and photoluminescent properties of Eu doped WO₃ film. *Electrochim. Acta* **278**, 263–270 (2018).
- Zheng, T. et al. Conductive tungsten oxide nanosheets for highly efficient hydrogen evolution. *Nano Lett.* **17**, 7968–7973 (2017).
- Mir, R. A., Kaur, G. & Pandey, O. Facile process to utilize carbonaceous waste as a carbon source for the synthesis of low cost electrocatalyst for hydrogen production. *Int. J. Hydrog. Energy* **45**, 23908–23919 (2020).

47. Malakzadeh, M., Raoof, J. B., Ghafarnejad, A. & Ojani, R. In-situ electrosynthesis Cu-PtBTC MOF-derived nanocomposite modified glassy carbon electrode for highly performance electrocatalysis of hydrogen evolution reaction. *J. Electroanal. Chem.* **900**, 115716 (2021).
48. Pan, J. et al. A high-performance electrochromic device assembled with hexagonal WO₃ and NiO/PB composite nanosheet electrodes towards energy storage smart window. *Sol. Energy Mater. Sol. Cells* **207**, 110337 (2020).
49. Liang, J. et al. Nano WO₃-catalyzed one-pot process for mild oxidative depolymerization of lignin and its model compounds. *ChemCatChem* **13**, 3836–3845 (2021).
50. Kim, H.-S. et al. Oxygen vacancies enhance pseudocapacitive charge storage properties of MoO_{3-x}. *Nat. Mater.* **16**, 454–460 (2017).
51. Wang, J., Polleux, J., Lim, J. & Dunn, B. Pseudocapacitive contributions to electrochemical energy storage in TiO₂ (anatase) nanoparticles. *J. Phys. Chem. C* **111**, 14925–14931 (2007).
52. Paulsen, A. L., Kalamounias, A. G., Berg, R. W. & Boghosian, S. Raman spectroscopic study of tungsten (VI) oxosulfato complexes in WO₃-K₂S₂O₇-K₂SO₄ molten mixtures: stoichiometry, vibrational properties, and molecular structure. *J. Phys. Chem. A* **115**, 4214–4222 (2011).
53. Xie, C. et al. In-situ phase transition of WO₃ boosting electron and hydrogen transfer for enhancing hydrogen evolution on Pt. *Nano Energy* **71**, 104653–104660 (2020).
54. Mitchell, J. B. et al. Transition from battery to pseudocapacitor behavior via structural water in tungsten oxide. *Chem. Mater.* **29**, 3928–3937 (2017).
55. Chen, W. et al. Activity origins and design principles of nickel-based catalysts for nucleophile electrooxidation. *Chem* **6**, 2974–2993 (2020).
56. Lu, Y. et al. Identifying the geometric site dependence of spinel oxides for the electrooxidation of 5-hydroxymethylfurfural. *Angew. Chem. Int. Ed.* **59**, 19215–19221 (2020).

Acknowledgements

We are grateful for the financial support from the National Key R&D Program of China (2021YFB3801600), the National Natural Science Foundation of China (21872121, 21908189), the Fundamental Research Funds for the Central Universities (2017XZZX002-16), Ministry of Education of Singapore (Tier 1: RG4/20 and Tier 2: MOET2EP10120-0002), and Agency for Science, Technology and Research (AME IRG: A20E5c0080).

Author contributions

Y.W. and B.L. conceived the study. J.C., C.C. and M.Q. designed the experiment and performed the initial tests. J.C., Q.M., B.Lin, B.Li and H.Y. conducted the theoretical calculations. J.C., C.C. and M.Q. wrote the manuscript. All authors discussed the results and commented on the manuscript.

Competing interests

The authors declare no competing interests.

Additional information

Supplementary information The online version contains supplementary material available at <https://doi.org/10.1038/s41467-022-33007-3>.

Correspondence and requests for materials should be addressed to Bin Liu or Yong Wang.

Peer review information *Nature Communications* thanks Arik Beck and the other, anonymous, reviewer(s) for their contribution to the peer review of this work. Peer reviewer reports are available.

Reprints and permission information is available at <http://www.nature.com/reprints>

Publisher's note Springer Nature remains neutral with regard to jurisdictional claims in published maps and institutional affiliations.

Open Access This article is licensed under a Creative Commons Attribution 4.0 International License, which permits use, sharing, adaptation, distribution and reproduction in any medium or format, as long as you give appropriate credit to the original author(s) and the source, provide a link to the Creative Commons license, and indicate if changes were made. The images or other third party material in this article are included in the article's Creative Commons license, unless indicated otherwise in a credit line to the material. If material is not included in the article's Creative Commons license and your intended use is not permitted by statutory regulation or exceeds the permitted use, you will need to obtain permission directly from the copyright holder. To view a copy of this license, visit <http://creativecommons.org/licenses/by/4.0/>.

© The Author(s) 2022